# Correlation effects and hidden spin-orbit entangled electronic order in parent and electron-doped iridates $Sr_2IrO_4$

Sen Zhou[1,2], Kun Jiang[3], Hua Chen[4], and Ziqiang Wang[3]
[1]*CAS Key Laboratory of Theoretical Physics, Institute of Theoretical Physics, Chinese Academy of Sciences, Beijing 100190, China*
[2]*School of Physical Sciences, University of Chinese Academy of Sciences, Beijing 100049, China*
[3]*Department of Physics, Boston College, Chestnut Hill, Massachusetts 02467, USA and*
[4]*International Center for Quantum Materials and School of Physics, Peking University, Beijing 100871, China*
(Dated: May 22, 2019)

Electron correlation effects are essential in $5d$ perovskite iridiates due to the strong spin-orbit coupling on Ir atoms. Recent experiments discovered possible hidden order in the parent antiferromagnetic (AF) insulator $Sr_2IrO_4$, the bulk electron doped paramagnetic (PM) metal $Sr_{2-x}La_xIrO_4$ with Fermi surface pockets, and a Fermi arc pseudogap under surface electron doping. Here, we provide a description of these highly spin-orbit entangled electronic states by studying correlation and disorder effects in a five-orbital model derived from the band theory. We find that the experimental observations are consistent with an electronic order that breaks the joint two-fold spin-orbital rotation followed by a lattice translation and corresponds to a $d$-wave $J_{\rm eff} = 1/2$ pseudospin current. It gaps out the quadratic band touching at momentum $X = (\pi, 0)$, $(0, \pi)$ and generates electron pockets in the PM phase and splits the degenerate band near $X$ in the canted AF insulator, in remarkable agreement with experiments. The disorder effects are discussed in connection to the observed pseudogap and Fermi arcs.

The iridium oxide $Sr_2IrO_4$, isostructural to the high-$T_c$ cuprates $La_2CuO_4$, is a canted AF insulator below a Néel temperature $T_N \simeq 230$ K [1, 2]. The canting of the in-plane magnetic moments tracks the $\theta \simeq 11^\circ$ staggered $IrO_6$ octahedra rotation about the $c$ axis [3–6] under the strong spin-orbit coupling (SOC). The AF insulating state arises from a novel interplay between electron correlation and strong SOC most easily understood near the atomic limit. $Ir^{4+}$ has a $5d^5$ configuration. The 5 electrons occupy the lower 3-fold $t_{2g}$ orbitals separated from the higher 2-fold $e_g$ orbitals by the cubic crystal field $\Delta_c$. The strong atomic SOC, $\lambda_{\rm soc}$, splits the $t_{2g}$ orbitals into a low-lying $J_{\rm eff} = 3/2$ spin-orbit multiplet fully occupied by 4 electrons and a $J_{\rm eff} = 1/2$ doublet hosting the remaining electron. Assuming $\lambda_{\rm soc}$ and $\Delta_c$ are sufficiently large compared to the relevant bandwidths when $Sr_2IrO_4$ crystalizes, a remarkable situation arises: a narrow single $J_{\rm eff} = 1/2$ band becomes half-filled and can be driven by a moderate local Coulomb repulsion $U$ to an AF Mott insulating state [1, 2, 7]. Moreover, carrier doping such an AF insulating state was proposed to potentially realize a $5d$ $t_{2g}$-electron analog of the $3d$ $e_g$-electron high-$T_c$ cuprate superconductors [8–12]. The situation in real crystals are complicated since these energy scales are comparable. The nature of the spin-orbit entangled insulating state is actively investigated using the localized picture based on the $J_{\rm eff} = 1/2$ pseudospin anisotropic Heisenberg model [7, 9, 13–15], the three-orbital Hubbard model for the $t_{2g}$ electrons with SOC [10, 11, 16, 17], and the microscopic correlated density functional theory such as the LDA+U and GGA+U [1, 18–20].

The focus of this work is the increasing evidence for hidden order in both stoichiometric and electron-doped $Sr_2IrO_4$. First of all, the canted AF order alone cannot fully describe the insulating ground state of $Sr_2IrO_4$. Neutron and resonant X-ray scattering observed additional symmetry breaking patterns [21–23] unaccounted for to date. Recent optical harmonic generation measurements discovered a hidden order below 170 K that breaks both rotational and spatial inversion symmetry, and is consistent with an odd-parity intra-cell loop current [24]. We will point out additional evidence from the quasiparticle (QP) dispersion in the canted AF insulator by high resolution angle-resolved photoemission (ARPES) [25] that revealed a degeneracy splitting near the high symmetry point $X = (\pi, 0)$ and $(0, \pi)$, indicative of a symmetry breaking hidden electronic order. Furthermore, electron doping has been achieved recently by La substitution ($Sr_{2-x}La_xIrO_4$) [25, 26], oxygen deficiency ($Sr_2IrO_{4-\delta}$) [27], and *in situ* potassium surface doping [28–30]. ARPES shows that the collapse of the insulating gap, consistent with the suppression of AF order, gives rise to a PM metallic state with Fermi surface pockets for bulk doping at $x = 0.1$ [25] and to Fermi arcs [28] with $d$-wave like pseudogaps [25, 29] for surface doping. We show that these remarkable properties of the low-energy QP excitations, some strikingly analogous to those in hole doped high-$T_c$ cuprates, can be described by a spin-orbit entangled electronic order associated with the $d$-wave $J_{\rm eff} = 1/2$ pseudospin current that breaks the symmetry of two-fold spin-orbital rotation followed by lattice translation and may play an important role for understanding the imminent superconducting phase suggested by the recent STM experiments [30].

We start with a realistic electronic structure calculation within the local density approximation (LDA) including SOC and the structural distortion [31, 32]. The result is shown in Fig. 1a for $\theta = 11^\circ$. We then construct a two-dimensional tight-binding model including SOC (TB+SOC) for the low-energy band

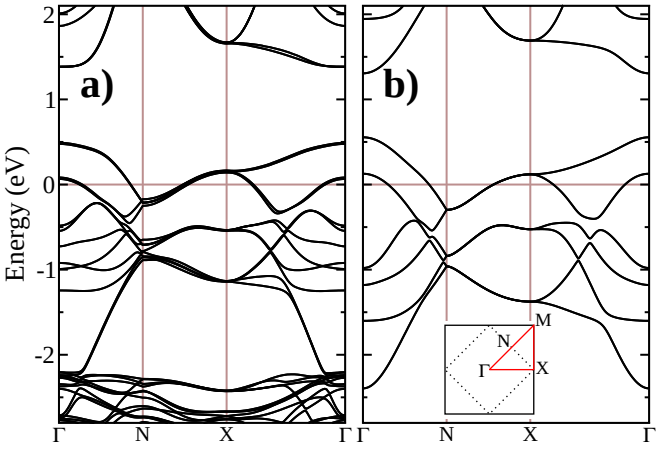


FIG. 1: Comparison of the band structures obtained using (a) LDA and (b) the five-orbital TB+SOC model with lattice distortion caused by staggered octahedra rotation. The doubling of bands and the small band splitting in (a) is due to the doubling of unit cell along $c-$axis. The inset in (b) shows the one-Ir Brillouin zone (solid black lines), the reduced zone (dotted black lines), and the high-symmetry points labeled by $\Gamma=(0,0)$, $X=(\pi,0)$, $M=(\pi,\pi)$, and $N=(\pi/2,\pi/2)$.

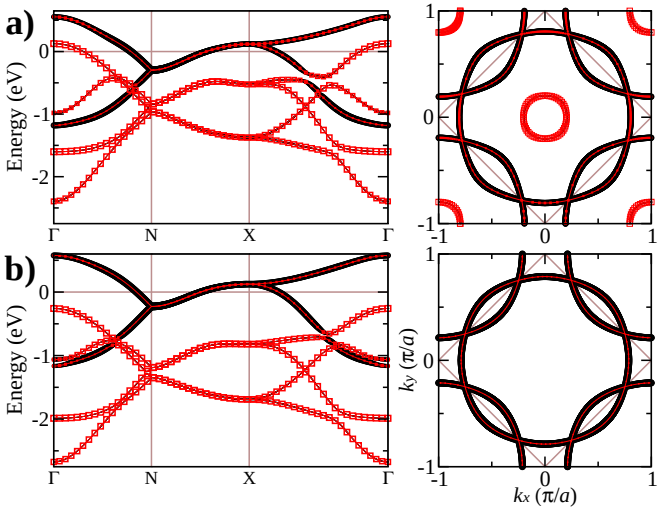


FIG. 2: The band dispersions and the corresponding FS of (a) the noninteracting $U=0$ and (b) the nonmagnetic state in the interacting $(U,J)$=(1.2, 0.05) eV system at $x=0$. The thickness of the black lines denotes the content of the $J_{\rm eff}=1/2$ doublet, while the size of the red open squares shows the content of the $J_{\rm eff}=3/2$ multiplet.

structure using five localized Wannier orbitals labeled by $\mu=1(d_{YZ}),2(d_{ZX}),3(d_{XY}),4(d_{3Z^2-R^2}),5(d_{X^2-Y^2})$. The TB+SOC Hamiltonian in the *local coordinates* that rotate with the octahedra is given by

$$\mathcal{H}_0=\sum_{ij,\mu\nu,\sigma}t_{ij}^{\mu\nu,\sigma}d_{i\mu\sigma}^\dagger d_{j\nu\sigma}+\sum_{i\mu\sigma}\epsilon_\mu d_{i\mu\sigma}^\dagger d_{i\mu\sigma}+\sum_{i,\mu\nu,\sigma\sigma'}\lambda_{\rm soc}\left\langle\mu\left|\mathbf{L}\right|\nu\right\rangle\cdot\left\langle\sigma\left|\mathbf{S}\right|\sigma'\right\rangle d_{i\mu\sigma}^\dagger d_{i\nu\sigma'}. \quad (1)$$

Here $d_{i\mu\sigma}^\dagger$ creates an electron with spin-$\sigma$ in the $\mu$-th orbital at site $i$, and $t_{ij}^{\mu\nu,\sigma}$ is the spin-and-orbital dependent complex hopping integrals between sites $i$ and $j$ of up to fifth nearest neighbors given in the Supplemental Material [33]. The second term in Eq. (1) denotes the crystalline electric field (CEF) $\epsilon_{1,\cdots,5}=(0,0,202,3054,3831)$meV determining the hierarchy of atomic states in the elongated $IrO_6$ octahedra with a separation of $\Delta_c\equiv 10Dq\approx 3.4$eV between the $t_{2g}$ and $e_g$ complexes. The last term in Eq. (1) is the atomic SOC with $\lambda_{\rm soc}=357$ meV and $\mathbf{L}$ and $\mathbf{S}$ the orbital and spin angular momentum operators respectively. In the five $d$-orbital basis, the matrix element $L_{\mu\nu}^\eta=\langle\mu\left|L^\eta\right|\nu\rangle$ is given explicitly in the Supplemental Material [33]. In spin space $S_{\sigma\sigma'}^\eta=\langle\sigma\left|S^\eta\right|\sigma'\rangle=\frac{1}{2}\tau_{\sigma\sigma'}^\eta$ where $\eta=x,y,z$ and $\tau^\eta$ are the Pauli matrices. The band dispersion produced by the TB+SOC Hamiltonian is shown in Fig. 1b, which captures faithfully the LDA band structure in Fig. 1a near the Fermi level. Zooming in to low energies in Fig. 2a, it is clear that for the realistic bandwidths and CEF, the atomic SOC is insufficient to prevent two bands of predominantly $J_{\rm eff}=1/2$ and $3/2$ characters to cross the Fermi level and give rise to two Fermi surfaces (FS) shown in Fig. 2(a).

To study the electron correlation effects, we consider the five-orbital Hubbard model $\mathcal{H}=\mathcal{H}_0+\mathcal{H}_U$ with

$$\mathcal{H}_U=U\sum_{i,\mu}\hat{n}_{i\mu\uparrow}\hat{n}_{i\nu\downarrow}+(U'-J/2)\sum_{i,\mu<\nu}\hat{n}_{i\mu}\hat{n}_{i\nu}-J\sum_{i,\mu\neq\nu}\mathbf{S}_{i\mu}\cdot\mathbf{S}_{i\nu}+J\sum_{i,\mu\neq\nu}d_{i\mu\uparrow}^\dagger d_{i\mu\downarrow}^\dagger d_{i\nu\downarrow}d_{i\nu\uparrow}, \quad (2)$$

where $U$ and $U'$ are the local intra- and inter-orbital Coulomb repulsions and $J$ is the Hund's rule coupling with $U=U'+2J$. In the presence of SOC, the Hartree and exchange self energies induced by $\mathcal{H}_U$ depend on the full spin-orbital dependent density matrix $n_{i\sigma\sigma'}^{\mu\nu}=\langle d_{i\mu\sigma}^\dagger d_{i\nu\sigma'}\rangle$. Local physical quantities in the ground state can be expressed in terms of $n_{\sigma\sigma'}^{\mu\nu}$ and the tensor product $O\otimes\tau$, where $O$ denotes the set of SU(5) generators for Hermitian matrices in the orbital space. For example, the orbital occupation $n_\mu=\sum_\sigma n_{\sigma\sigma}^{\mu\mu}$; the spin density $S^\eta=\frac{1}{2}\sum_{\mu,\sigma\sigma'}\tau_{\sigma\sigma'}^\eta n_{\sigma\sigma'}^{\mu\mu}$; the orbital angular momentum $L^\eta=\sum_{\mu\neq\nu,\sigma}n_{\sigma\sigma}^{\mu\nu}L_{\mu\nu}^\eta$ where the angular momentum matrices $L_{\mu\nu}^\eta$ are related to three antisymmetry generators in $O$; and the SOC $\Lambda^\eta=\frac{1}{2}\sum_{\mu\nu,\sigma\sigma'}n_{\sigma\sigma'}^{\mu\nu}L_{\mu\nu}^\eta\tau_{\sigma\sigma'}^\eta$. Carrying out the self-consistent calculations of the Hartree and exchange self energies, we found that the only corrections to the electronic structure in the absence of symmetry breaking ($\langle\mathbf{S}\rangle=\langle\mathbf{L}\rangle=0$) are the modification of the CEF and the renormalization of the the atomic SOC. However, due to the cubic crystal field, $\Lambda^\eta$ are not the same along the crystal directions. As a result, the correlation induced SOC renormalization is both directional and orbital dependent, *i.e.* the $\lambda_{\rm so}$ in Eq. (1) is replaced

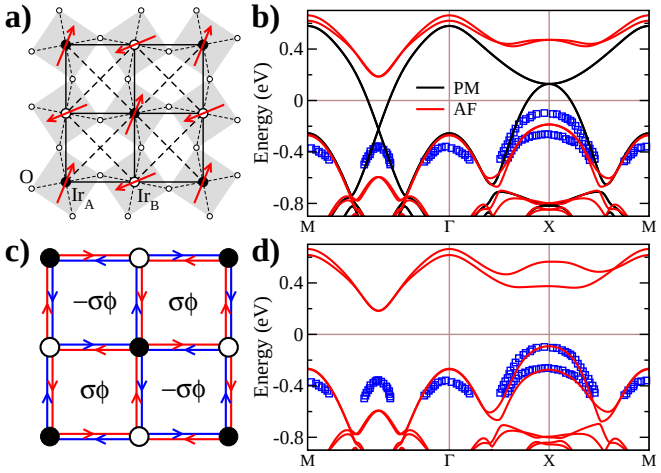


FIG. 3: (a) Schematics of the in-plane canted AF moments on the Ir square lattice with a two-dimensional rendering of the staggered $IrO_6$ octahedral rotation. (b) QP band dispersion in the canted AF state (red solid lines) and the nonmagnetic state (black solid lines) at $(U, J)$=(1.2, 0.05) eV and $x = 0$. (c) Schematics of the $d$-wave $J_{\rm eff} = 1/2$ pseudospin current order and associated staggered pseudospin flux $\Phi_\sigma = \pm\sigma\phi$. (d) QP band dispersion in the canted AF state with coexisting $d$-wave $J_{\rm eff} = 1/2$ pseudospin current corresponding to $\Delta_d = 30$meV. Open blue squares are data from ARPES experiments [25].

by $\lambda^\eta_{\mu\nu} = \lambda_{\rm soc} + \Delta\lambda^\eta_{\mu\nu}$ where $\Delta\lambda \propto (U' - J)$. Since $J$ is relatively small in the iridium $5d^5$ configuration, the correction to atomic SOC by local electron correlations is significant for $Sr_2IrO_4$.

*Interacting electronic structure.* In Fig. 2b, the interacting electronic structure is shown at $(U, J)$=(1.2, 0.05) eV and $x = 0$. We find that the most important correlation effect on the electronic structure is the renormalization of $\lambda_{\rm soc}$ discussed above, leading to a significantly enhanced effective SOC of 665 meV for the $t_{2g}$ complex, which is much larger than the bare atomic value. As a consequence, the $J_{\rm eff} = 3/2$ band in the LDA band structure in Fig. 2a is pushed below the Fermi level together with the hole FS pockets around $\Gamma$ and $M$, leading to a single band crossing the Fermi level as shown in Fig.2b, folded by $(\pi, \pi)$ due to the lattice distortion, that is at *half-filling* and of dominant $J_{\rm eff} = 1/2$ character. This correlation induced band polarization is due to the enhancement of the SOC by the Hubbard interactions - a mechanism that enables the $J_{\rm eff} = 1/2$ picture.

*Canted AF insulator at $x = 0$.* The fully self-consistent Hartee-Fock ground state at nonzero values of $U$ and $J$ is indeed a canted AF insulator as depicted in Fig. 3a. The magnetization and the canting angle depend on the interaction parameters. For $(U, J) = (1.2, 0.05)$eV the total ordered moment is estimated as $|\langle \mathbf{L}\rangle + 2\langle \mathbf{S}\rangle| \simeq 0.67\mu_B$ with a canting angle of about 22°, which are larger than experimental values since Hartee-Fock like weak-coupling approaches overestimate magnetism and the results should be regarded as qualitative rather than quantitative. Nevertheless, we find that the calculated QP dispersions plotted in Fig. 3b (red-solid lines) are quite robust and not sensitive to the values of the canting angle [34]. The AF gap opens fully from the nonmagnetic case (black lines) and the dispersion below the gap agrees overall with ARPES in undoped $Sr_2IrO_4$ [25]. However, there exists an important difference near the high symmetry point $X$: ARPES observes two split bands separated by about 200 meV as shown by the blue squares superimposed in Fig. 3b. A symmetry analysis is necessary to understand this difference. In the PM state, there exists a quadratic band touching (QBT) point located at $X$ in Fig. 3b, about 130meV above the Fermi level. This is a four-fold degenerate crossing point of the $J_{\rm eff} = 1/2$ doublet band with its $(\pi, \pi)$-folded counter part by the structural distortion. The SOC does not affect the band degeneracy at $X$. Although the AF order breaks the time-reversal ($\mathcal{T}$) symmetry and splits the Kramers pair by the AF gap, the corresponding QP band below the gap shown in Fig. 3b still maintains a two-fold degeneracy. The two split bands observed by ARPES near $X$ are thus consistent with a ±100 meV band degeneracy lifting due to an additional symmetry breaking associated with a hidden order in the canted AF state.

*Symmetry analysis: hidden order in AF phase.* The symmetry implications on the electronic structure of $Sr_2IrO_4$ are subtle because of the SOC that renders the point group incomplete. In the absence of SOC, the doubly-degenerate band in a two-sublattice collinear AF state on a bipartite lattice is related to a symmetry operation that rotates the spin by 180° ($R_s(\pi)$) followed by an $A \leftrightarrow B$ sublattice translation $\tau_{AB}$ [35]. In the iridates, spin rotations are coupled to orbital spatial rotations due to the strong SOC. As a consequence, $R_s(\pi)$ around the $[1\bar{1}0]$ axis (direction of the canted FM moment) indicated in Fig. 3a must be accompanied by a spatial $C_2'$ rotation around the same axis, leading to the joint two-fold rotation $\mathcal{J}_2' \equiv R_s(\pi) \otimes C_2'$. As a result, the corresponding symmetry operation in the spin-orbit entangled states must be extended to $\mathcal{R}_2' \equiv \mathcal{J}_2' \otimes \tau_{AB} = R_s(\pi) \otimes C_2' \otimes \tau_{AB}$. $\mathcal{R}_2'$ is indeed a symmetry *even in the presence of spin canting and the structural distortion.* Thus, the hidden spin-orbit entangled long-range order capable of lifting the two-fold band degeneracy near $X$ must spontaneously break $\mathcal{R}_2'$. The specific form of the latter can be determined by exhausting all possible interactions involving the low energy $t_{2g}$ orbitals that do not break lattice translation, identifying those that break $\mathcal{R}_2'$, examining the momentum space anisotropy of the resulting band degeneracy lifting and compare to the experiments [36]. Since the low energy physics here is dominated by the $J_{\rm eff} = 1/2$ quantum states, the outcome can be suitably understood in the local pseudospin basis [33] $|J = 1/2, J_z = \pm 1/2\rangle = \gamma^\dagger_\pm|0\rangle$ where,

$$\gamma_\sigma = \frac{1}{\sqrt{3}}\left(i\sigma d_{YZ,\bar{\sigma}} + d_{ZX,\bar{\sigma}} + i d_{XY,\sigma}\right), \qquad (3)$$

creates the $J_{\rm eff} = 1/2$ doublets in the low energy QP

excitations. Under the joint two-fold spin-orbital rotation $\mathcal{J}_2'^{\dagger}\gamma_\sigma^\dagger\gamma_\sigma\mathcal{J}_2' = \gamma_{\bar\sigma}^\dagger\gamma_{\bar\sigma}$, *i.e.* the pseudospin current $J_z \to -J_z$. Considering the spatial $C_2'$ and the sublattice translation $\tau_{AB}$, we arrive at the interaction that breaks the $\mathcal{R}_2'$ with the desired band degeneracy lifting,

$$\mathcal{H}_\Delta = i\Delta_d \sum_{i\in A,\sigma}\sum_{j=i+\delta} (-1)^{i_y+j_y}\sigma\gamma_{i,\sigma}^\dagger\gamma_{j,\sigma} + h.c. \qquad (4)$$

where $\delta = \pm\hat{x}, \pm\hat{y}$ and $(-1)^{i_y+j_y}$ is the standard nearest neighbor (nn) $d$-wave form factor. $\mathcal{H}_\Delta$ maintains $\mathcal{T}$, but breaks $\mathcal{R}_2'$ since $\mathcal{R}_2'^{\dagger}\mathcal{H}_\Delta\mathcal{R}_2' = -\mathcal{H}_\Delta$. It is precisely the $d$-wave $J_{\rm eff} = 1/2$ *pseudopsin current* order (d-PSCO) parameter, and an nonzero expectation value of $\mathcal{H}_\Delta$ gives rise to the "hidden" $J_{\rm eff} = 1/2$ d-PSCO, with staggered pseudospin plaquette flux for each component in opposite directions, as shown in Fig. 3c. This is one of the central results in this work. Note that $\mathcal{H}_\Delta$ can also be interpreted as a $d$-wave pseudospin orbital coupling (pSOC) and the $d$-wave form factor is crucial for breaking $\mathcal{R}_2'$. Indeed, projecting the tight-binding $\mathcal{H}_0$ into the $J_{\rm eff} = 1/2$ basis in the local coordinates generates an $s$-wave pSOC due to the structural distortion [8], which is invariant under $\mathcal{R}_2'$ and already present in the band theory. Including $\mathcal{H}_\Delta$ in the total Hamiltonian $\mathcal{H} = \mathcal{H}_0 + \mathcal{H}_U + \mathcal{H}_\Delta$, the canted AF phase at $x = 0$ indeed exhibits d-PSCO order for remarkably small $\Delta_d$, indicative of its propensity toward coexisting d-PSCO order. The calculated QP dispersion is shown in Fig. 3d for $\Delta_d = 30$ meV, which produces a $\pm 100$ meV degeneracy splitting in remarkable agreement with experiments [25]. The nn correlator of the $J_{\rm eff} = 1/2$ QP has the form $\chi_{ij}^\sigma = \chi_{ij}' + i\sigma\chi_{ij}''$. The pseudospin flux is thus $\Phi_\sigma = \pm\sigma\phi$, $\phi = \sum_\square \tan^{-1}(\chi_{ij}''/\chi_{ij}') \simeq 0.055\pi$. The QP number current on a link is $J_{ij}^\sigma \propto {\rm Im}\chi_{ij}^\sigma$, such that the pseudospin current $J_{ij}^{\rm ps} = \sum_\sigma \sigma J_{ij}^\sigma \neq 0$, whereas the charge current $J_{ij} = \sum_\sigma J_{ij}^\sigma = 0$, giving rise to the novel $\mathcal{T}$ symmetric state of spontaneously generated $d$-wave pseudospin current. The momentum space $d$-wave form factor $(\cos k_x - \cos k_y)$ ensures that the splitting is largest at $X$, and vanishes along the $\Gamma - M$ path in the BZ in agreement with the superimposed ARPES data. We note in passing that other $\mathcal{R}_2'$-breaking interactions capable of lifting the degeneracy at $X$ also break $\mathcal{T}$ or are strongly nematic and produce band dispersions incompatible with the experimental findings. It is remarkable, as we will show next, that the novel spin-orbit entangled and intertwined order in the canted AF phase can also account for the pseudogap phenomena in the PM phase following the collapse of the AF insulating gap in electron doped $Sr_2IrO_4$.

*Electron doped PM state at $x = 0.1$.* The calculated QP band dispersions at $x = 0.1$ in the PM state and in the absence of $\mathcal{H}_\Delta$ are shown in Fig. 4a for $(U, J)$=(1.4, 0) eV. Note that despite the absence of AF order, the bands are still folded by $(\pi, \pi)$ due to the staggered $IrO_6$ octahedra rotation. Moreover, the 10% *electron* doping moves the Fermi energy ($E_F$) upward to within 70meV of the QBT at $X$ in Fig. 4a. Comparing to the superimposed dispersion measured by ARPES [25], the electron FS pocket in Fig. 4b is indeed observed around $(\pi/2, \pi/2)$ with the QP dispersion extending from $E_F$ down to and beyond the "Dirac crossing", consistent with the calculated QP dispersion in Fig. 4a. However, the hole FS pocket around $X$ in Fig. 4b was not observed by ARPES; the measured QP peak near $X$ follows the band dispersion below $E_F$ in Fig. 4a but loses its intensity before reaching the Fermi level, leading to the emergence of a pseudogap of about 30 meV at the $X$ point [25]. It is natural to suspect that the collapse of the AF long-range order and the associated insulating gap with electron doping would leave behind short-range AF order or fluctuations [37, 38] responsible for the pseudogap near $X$ [39]. This is however unlikely since the latter would have produced a significant energy gap in the QP dispersion around $(\pi/2, \pi/2)$ as well which was not detected by ARPES [25].

We propose that closing of the AF gap by electron doping reveals the novel d-PSCO in Eq. (4) already present in the canted AF phase. A gap opening at $X$ requires symmetry breaking and lifting the degeneracy of the QBT, which is analogous to the situation in topological semimetals where the QBT also occurs [40, 41]. In pyrochlore iridates $Pr_2Ir_2O_7$, gapping out the QBT at BZ center has topological implications in the resulting insulating phase [42]. In $Sr_2IrO_4$, the $\mathcal{T}$ symmetry in the PM phase protects the Kramers degeneracy of the QBT at $X$. However, the proximity of the QBT to $E_F$ makes it prone to d-PSCO that spontaneously breaks the $\mathcal{R}_2'$ symmetry and thus lifts the remaining two-fold degeneracy and gaps out the QBT. Fig. 4d shows the calculated QP dispersion in the presence of the $J_{\rm eff} = 1/2$ d-PSCO described by $\mathcal{H}_\Delta$ in Eq. (4) with an identical magnitude $\Delta_d = 30$meV used in the AF phase at $x = 0$. The induced staggered pseudospin flux is $\pm\sigma\phi$ with $\phi = 0.589\pi$. The d-PSCO order splits the QBT by about 200meV and produces a 30meV gap in the QP dispersion around $X$, leaving behind only the electron pocket around $(\pi/2, \pi/2)$ (Fig. 4e) occupied by the doped carriers. The $d$-wave form factor ensures that the hidden d-PSCO only affects the electronic structure around $X$ such that the QP dispersions and the associated electron FS pockets shown in Figs 4d and 4e are in remarkable agreement with the ARPES data in bulk electron-doped $Sr_2IrO_4$ [25]. Fig. 4f shows that the QP spectral weight is much larger on the outer than on the inner halves of the FS pockets, consistent with the former being the main $J_{\rm eff} = 1/2$ QP band while the latter the folded band (see Fig. 4c) due to the structural distortion and d-PSCO order. Indeed, significant photon energy dependent spectral weight anisotropy on the electron pocket has been observed in by ARPES. The current theory, however, cannot explain the surprising result that at certain photon energies, the folded portion has higher intensity which may be caused by complicated matrix element effects [25]. A closer look at the band dispersion near $X$ in Fig. 4d reveals a weak asymmetry along the directions $\Gamma \to X$ and $X \to M$ related by 90° rota-

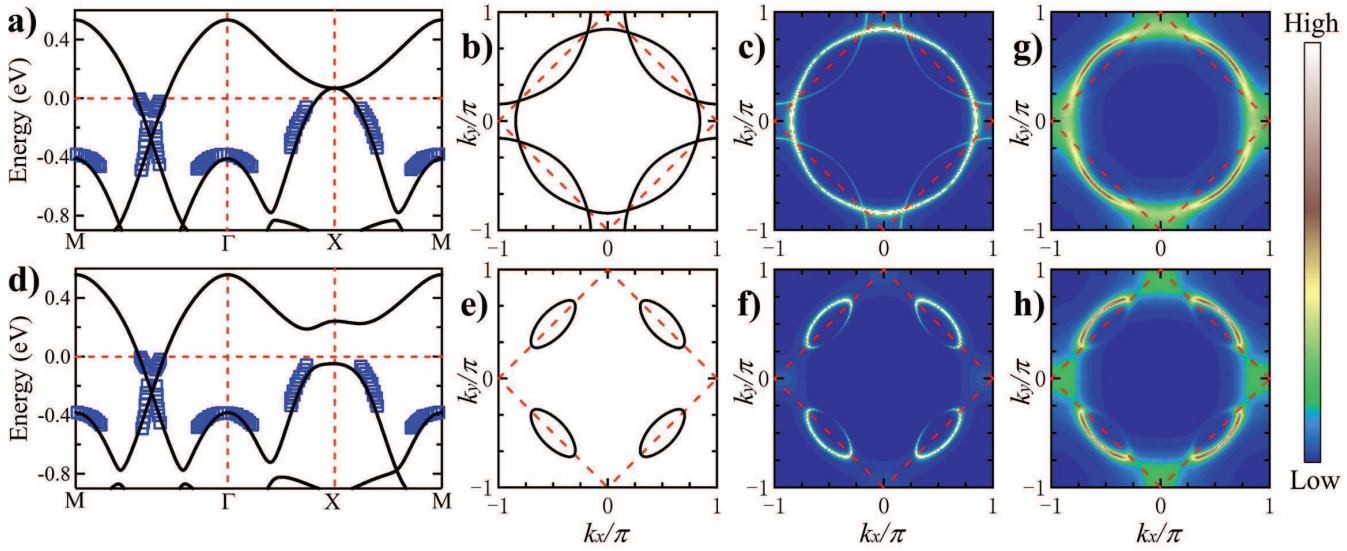


FIG. 4: The PM phase at $x = 0.1$ and $(U, J)$=(1.4, 0) eV.(a) Band dispersion in the absence $H_\Delta$, i.e without d-PSCO (black lines), (b) corresponding FS, and (c) spectral weight over the FS. (d) Band dispersion in the presence of d-PSCO for $\Delta_d = 30$meV showing the gapping of the QBT at $X$ (red lines), (e) corresponding FS, and (f) spectral weight over the FS. (g) FS in the presence of disorder with $\Delta_d = 0$ and $\varepsilon = 60$meV, showing the Fermi arcs in the $J_{\rm eff} = 1/2$ pseudospin current glass. (h) FS in the disordered d-PSCO with $\Delta_d = 30$meV and $\varepsilon = 60$meV. ARPES data [25] are superimposed as open blue squares.

tions. However, in the absence of structure distortion, the $J_{\rm eff} = 1/2$ d-PSCO does not break four-fold rotation ($C_4$ plus 90° spin rotation in the presence of SOC) since $\mathcal{J}_2' \otimes \mathcal{T}$ is still a good symmetry in both the PM and AF phases even in the presence of $H_\Delta$ that effectively interchanges $k_x \leftrightarrow k_y$, and the asymmetry in the dispersion would be absent. Thus, the weak asymmetry in the gapped QP dispersions near $X$ is due to the structure distortion that breaks $\mathcal{J}_2' \otimes \mathcal{T}$, causing a mixing the $s$-wave pSOC with the $d$-wave pseudospin current on the bonds, and is visible in the ARPES data in Fig. 4d. The same analysis applies to the split QP dispersion near $X$ in the canted AF phase shown in Fig. 3d.

*Disorder effects and surface doping.* Chemical doping by La in $Sr_{2-x}La_xIrO_4$ necessarily introduces disorder. Moreover, heavy K dosing is likely to increase the disorder at sample surfaces and cause additional disorder in the structure distortion. In high-$T_c$ cuprates, doping induced disorder contributes significantly to the observed electronic inhomogeneity [43–47]. Furthermore, when a system sits in proximity to certain long-range electronic order, disorder can pin quantum fluctuations to form a spatially inhomogeneous state with glassy or short-range order that inherits the spectroscopic properties of the ordered state. The $d$-wave valence bond glass is such an example proposed for the pseudogap phase with Fermi arcs in underdoped cuprates [48]. To model the disorder effects, we performed real space calculations where Eq. (4) is replaced by

$$\mathcal{H}_\Delta^{\rm dis} = i \sum_{i\in A,\sigma} \sum_{j=i+\delta} \Delta_{ij} \sigma \gamma_{i,\sigma}^\dagger \gamma_{j,\sigma} + h.c. \qquad (5)$$

where the bond coupling $\Delta_{ij} = (-1)^{i_y+j_y}\Delta_d + \delta\Delta_{ij}$ with $\Delta_d$ the average $d$-wave contribution and random $\delta\Delta_{ij}$ taken from a Gaussian distribution of zero mean and standard deviation $\varepsilon$. Note that the disordered $\delta\Delta_{ij}$ necessarily involve spatially fluctuating $J_{\rm eff} = 1/2$ $d$-wave pseudospin current and $s$-wave pSOC. We first set $\Delta_d = 0$, such that the $J_{\rm eff} = 1/2$ d-PSCO vanishes on average, $\langle \mathcal{H}_\Delta \rangle = 0$, but its moment $\langle \mathcal{H}_\Delta^2 \rangle \neq 0$, giving rise to a $J_{\rm eff} = 1/2$ $d$-wave valence bond current glass. The disorder averaged QP FS is calculated [49] at $x = 0.1$ with $\varepsilon = 60$meV and plotted in Fig. 4g, showing the destruction of the FS sections around $X$. More remarkable is the emergence of full fledged Fermi arcs as the folded part of the FS is destroyed by the scattering due to spatially fluctuating pseudospin current. This is consistent with the observed Fermi arcs supported by $d$-wave like pseudogaps by ARPES and STM in heavily surface K-doped $Sr_2IrO_4$ [28–30]. Fig. 4h is a spectral intensity plot of the FS when the disordered pseudospin current fluctuates spatially with $\varepsilon = 60$meV around a nonzero mean of the d-PSCO with $\Delta_d = \pm 30$ meV to account for averaging over two domains. Since the static order is comparable to the disorder strength, although the spectral weight on the inner halves of the electron pockets is suppressed, the bending over of the Fermi arcs remains visible.

*Summary and discussions* Supported by symmetry analysis and the agreement between the calculated QP dispersion and the ARPES experiments, we conjecture that the $\mathcal{T}$ symmetric but $\mathcal{R}_2'$ breaking $d$-wave $J_{\rm eff} = 1/2$ pseudospin current (flux) is a hidden electronic order in

perovskite iridates $Sr_{2-x}La_xIrO_4$. The d-PSCO offers a possible explanation of the splitting of the $J_{\rm eff} = 1/2$ QP bands near $X$ in the canted AF insulator at $x = 0$ and the gapping of the hole pocket around $X$ and the emergence of the electron FS pockets at $x = 0.1$ [25]. Moreover, disordered, spatially fluctuating pseudospin current can produce a glassy valence bond state supporting the observed Fermi arcs and pseudogap state in surface doped $Sr_2IrO_4$ [28–30]. Recent optical second harmonic generation experiments detected a rotation and inversion symmetry breaking hidden order below 170K [24]. Whether the observation is consistent with an odd-parity magnetic multipole order associated with an orbital current is under debate [24, 50]. Although the d-PSCO proposed here is overall not inconsistent with the observation, further studies are required to make more detailed connection. Finally, the nature of the nonlocal $d$-wave pseudospin bond current suggests that it may originate microscopically from intersite electronic interactions in $Sr_2IrO_4$. Indeed, Eq. (4) can be obtained by decoupling the nn interatomic Coulomb interaction $V$ between the $J_{\rm eff} = 1/2$ quasiparticles [51]. Thus, the d-PSCO can emerge from charge fluctuations of strongly spin-orbit coupled quasiparticles and may coexist with and/or participate in the suppression of the spin-orbit entangled magnetic order under electron doping. Such charge fluctuations may play an essential role in the possible emergence of superconductivity in $Sr_{2-x}La_xIrO_4$ [29, 30].

We thank Stephen Wilson for useful discussions. This work is supported by the U.S. Department of Energy, Basic Energy Sciences Grant No. DE-FG02-99ER45747 (Z.W.) and the Key Research Program of Frontier Sicences, CAS No. QYZDB-SSW-SYS012 (S.Z.). Numerical calculations were performed on HPC Cluster of ITP-CAS. Z.W. thanks the hospitality of Aspen Center for Physics and the support of ACP NSF grant PHY-1066293.

[1] B.J. Kim *et. al.*, Novel $J_{\rm eff} = 1/2$ Mott State Induced by Relativistic Spin-Orbit Coupling in $Sr_2IrO_4$, Phys. Rev. Lett. **101**, 076402 (2008).

[2] B.J. Kim *et. al.*, Phase-Sensitive Observation of a Spin-Orbital Mott State in $Sr_2IrO_4$, Science **323**, 1329 (2009).

[3] Q. Huang *et. al.*, Neutron Powder Diffraction Study of the Crystal Structures of $Sr_2RuO_4$ and $Sr_2IrO_4$ at Room Temperature and at 10 K, J. Solid State Chem. **112**, 355 (1994).

[4] R.J. Cava *et. al.*, Localized-to-itinerant electron transition in $Sr_2Ir_{1-x}Ru_xO_4$, Phys. Rev. B **49**, 11890 (1994).

[5] G. Cao, J. Bolivar, S. McCall, J.E. Crow, and R.P. Guertin, Weak ferromagnetism, metal-to-nonmetal transition, and negative differential resistivity in single-crystal $Sr_2IrO_4$, Phys. Rev. B **57**, 11039(R) (1998).

[6] M.K. Crawford *et. al.*, Structural and magnetic studies of $Sr_2IrO_4$, Phys. Rev. B **49**, 9198 (1994).

[7] G. Jackeli and G. Khaliullin, Mott Insulators in the Strong Spin-Orbit Coupling Limit: From Heisenberg to a Quantum Compass and Kitaev Models, Phys. Rev. Lett. **102**, 017205 (2009).

[8] Fa Wang and T. Senthil, Twisted Hubbard Model for $Sr_2IrO_4$: Magnetism and Possible High Temperature Superconductivity, Phys. Rev. Lett. **106** 136402 (2011).

[9] J.W. Kim *et. al.*, imensionality Driven Spin-Flop Transition in Layered Iridates, Phys. Rev. Lett. **109**, 037204 (2012).

[10] H. Watanabe, T. Shirakawa, and S. Yunoki, Microscopic Study of a Spin-Orbit-Induced Mott Insulator in Ir Oxides, Phys. Rev. Lett. **105**, 216410 (2010).

[11] H. Watanabe, T. Shirakawa, and S. Yunoki, Theoretical study of insulating mechanism in multiorbital Hubbard models with a large spin-orbit coupling: Slater versus Mott scenario in $Sr_2IrO_4$, Phys. Rev. B **89**, 165115 (2014).

[12] Z.-Y. Meng, Y.B. Kim, and H.-Y. Kee, Odd-Parity Triplet Superconducting Phase in Multiorbital Materials with a Strong Spin-Orbit Coupling: Application to Doped $Sr_2IrO_4$, Phys. Rev. Lett. **113**, 177003 (2014).

[13] S. Fujiyama *et. al.*, Two-Dimensional Heisenberg Behavior of $J_{\rm eff} = 1/2$ Isospins in the Paramagnetic State of the Spin-Orbital Mott Insulator $Sr_2IrO_4$, Phys. Rev. Lett. **108**, 247212 (2012).

[14] N.B. Perkins, Y. Sizyuk, and P. Wölfle, Interplay of many-body and single-particle interactions in iridates and rhodates, Phys. Rev. B **89**, 035143 (2014).

[15] J.-M. Carter, V. Shankar V., and H.-Y. Kee, Theory of metal-insulator transition in the family of perovskite iridum oxides, Phys. Rev. B **88**, 035111 (2013).

[16] R. Arita, J. Kuneš, A.V. Kozhevnikov, A.G. Eguiluz, and M. Imada, *Ab initio* Studies on the Interplay between Spin-Orbit Interaction and Coulomb Correlation in $Sr_2IrO_4$ and $Ba_2IrO_4$, Phys. Rev. Lett. **108**, 086403 (2012).

[17] D. Hsieh, F. Mahmood, D.H. Torchinsky, G. Cao, and N. Gedik, Observation of a metal-to-insulator transition with both Mott-Hubbard and Slater characteristics in $Sr_2IrO_4$ from time-resolved photocarrier dynamics, Phys. Rev. B **86**, 035128 (2012).

[18] H. Jin, H. Jeong, T. Ozaki, and J.-J. Yu, Anisotropic exchange interactions of spin-orbit-integrated states in $Sr_2IrO_4$, Phys. Rev. B **80**, 075112 (2009).

[19] P.-T. Liu *et. al.*, Anisotropic magneti couplings and structure-driven canted to collinear transitions in $Sr_2IrO_4$ by magnetically constrained moncollinear DFT, Phys. Rev. B **92**, 054428 (2015).

[20] P.-T. Liu *et. al.*, Electron and hole doping in the relativistic Mott insulator $Sr_2IrO_4$: A first-principles study using band unfolding technique, Phys. Rev. B **94**, 195145 (2016).

[21] Feng Ye *et. al.*, Magnetic and crystal structures of $Sr_2IrO_4$: A neutron diffraction study, Phys. Rev. B **87**, 140406(R) (2013).

[22] Chetan Dhital *et. al.*, Neutron scattering study of correlated phase behavior in $Sr_2IrO_4$, Phys. Rev. B **87**, 144405 (2013).

[23] S. Boseggia *et. al.*, Robustness of Basal-Plane Antiferromagnetic Order and the $J_{\rm eff} = 1/2$ State in Single-Layer

Iridate Spin-Orbit Mott Insulators, Phys. Rev. Lett. **110**, 117207 (2013).
[24] L. Zhao *et. al.*, Evidence of an odd-parity hidden order in a spin-orbit coupled correlated iridate, Nat. Phys. **12**, 32 (2015).
[25] A. de la Torre *et. al.*, Collaps of the Mott Gap and Emergence of a Nodal Liuid in Lightly Doped $Sr_2IrO_4$, Phys. Rev. Lett. **115**, 176402 (2015).
[26] M.-Y. Li *et. al.*, Tuning the Electronic Structure of Thin Films by Bulk Electronic Doping Using Molecular Beam Epitaxy, Chin. Phys. Lett. **32**, 057402 (2015).
[27] O.B. Korneta *et. al.*, Electron-doped $Sr_2IrO_{4-\delta}$ ($0 \leq \delta \leq 0.04$): Evolution of a disordered $J_{\text{eff}} = \frac{1}{2}$ Mott insulator into an exotic metallic state, Phys. Rev. B **82**, 115117 (2010).
[28] Y.K. Kim *et. al.*, Fermi arcs in a doped pseudospin-1/2 Heisenberg antiferromagnet, Science **345**, 187 (2014).
[29] Y.K. Kim, N.H. Sung, J.D. Denlinger, and B.J. Kim, Observation of a *d*-wave gap in electron-doped $Sr_2IrO_4$, Nat. Phys. **12**, 37 (2016).
[30] Y.J. Yan *et. al.*, Electron-Doped $Sr_2IrO_4$: An Analogue of Hole-Doped Cuprate Superconductors Demonstrated by Scanning Tunneling Microscopy, Phys. Rev. X **5**, 041018 (2015).
[31] C. Martins, M. Aichhorn, L. Vaugier, and S. Biermann, Reduced Effective Spin-Orbital Degeneracy and Spin-Orbital Ordering in Paramagnetic Transition-Metal Oxides: $Sr_2IrO_4$ versus $Sr_2RhO_4$, Phys. Rev. Lett. **107**, 266404 (2011).
[32] P. Giannozzi *et. al.*, QUANTUM ESPRESSO: a modular and open-source software project for quantum simulations of materials, J. Phys.: Condens. Matter **39**, 395502 (2009).
[33] See Supplementary Material for details.
[34] We have checked that using the value of 11° for the canting angle, which is close to the measured value, does not give any appreciable change in the obtained band dispersion.
[35] E. Berg, C.-C. Chen, and S.A. Kivelson, Stability of Nodal Quasiparticles in Superconductors with Coexisting Orders, Phys. Rev. Lett. **100**, 027003 (2010).
[36] K. Jiang, J.-P. Hu, H. Ding, and Z. Wang, Interatomic Coulomb interaction and electron nematic bond order in FeSe, Phys. Rev. B **93**, 115138 (2016).
[37] X. Liu *et. al.*, Anisotropic softening of magnetic excitations in lightly electron-doped $Sr_2IrO_4$, Phys. Rev. B **93**, 241102(R) (2016).
[38] H. Gretarsson *et. al.*, Persistent Paramagnons Deep in the Metallic Phase of $Sr_{2-x}La_xIrO_4$, Phys. Rev. Lett. **117**, 107001 (2016).
[39] Hu Wang, Shun-Li Yu, and Jian-Xin Li, Fermi arcs, pseudogap, and collective excitations in doped $Sr_2IrO_4$: A generalized fluctuation exchange study, Phys. Rev. B **91**, 165138 (2015).
[40] Kai Sun, Hong Yao, Eduardo Fradkin, and S.A. Kivelson, Topological Insulators and Nematic Phases from Spontaneous Symmetry Breaking in 2D Fermi Systems with a Quadratic Band Crossing, Phys. Rev. Lett. **103**, 046811 (2009).
[41] E.-G. Moon, C. Xu, Y.B. Kim, and L. Balents, Non-Fermi-Liquid and Topological States with Strong Spin-Orbit Coupling, Phys. Rev. Lett. **111**, 206401 (2013).
[42] T. Kondo *et. al.*, Quadratic Fermi node in a 3D strongly correlated semimetal, Nat. Commun. **6** 10042 (2015).
[43] S.H. Pan *et. al.*, Microscopic electronic inhomogeneity in the high-Tc superconductor $Bi_2Sr_2CaCu_2O_{8+x}$, Nature **413**, 282 (2001).
[44] Z. Wang, J.R. Engelbrecht, S.C. Wang, H. Ding, and S.H. Pan, Inhomogeneous *d*-wave superconducting state of a doped Mott insulator, Phys. Rev. B **65**, 064509 (2002).
[45] K. McElroy, J. Lee, J. A. Slezak, D.-H. Lee, H. Eisaki, S. Uchida, and J. C. Davis, Atomic-Scale Sources and Mechanism of Nanoscale Electronic Disorder in $Bi_2Sr_2CaCu_2O_{8+\delta}$, Science **309**, 1048 (2005).
[46] Sen Zhou, Hong Ding, and Ziqiang Wang, Correlating Off-Stoichiometric Doping and Nanoscale Electronic Inhomogeneity in the High-$T_c$ Superconductor $Bi_2Sr_2CaCu_2O_{8+\delta}$, Phys. Rev. Lett. **98**, 076401 (2007).
[47] I. Zeljkovic, Z. Xu, J.S. Wen, G.D. Gu, R.S. Markiewicz, and J.E. Hoffman, Imaging the Impact of Single Oxygen Atoms on Superconducting $Bi_2Sr_2CaCu_2O_{8+x}$, Science **337**, 320 (2012).
[48] Liang Ren Niestemski and Ziqiang Wang, Valence Bond Glass Theory of Electronic Disorder and the Pseudogap State of High-Temperature Cuprate Superconductors, Phys. Rev. Lett. **102**, 107001 (2009).
[49] We average over 40 disorder realizations on samples of 20×20 sites. To reduce the finite size effects, for each disorder realization, we average over different boundary conditions corresponding to 10×10 supercells.
[50] S.D. Matteo and M.R. Norman, Magnetic ground state of $Sr_2IrO_4$ and implications for second-harmonic generation, Phys. Rev. B **94**, 075148 (2016).
[51] S. Raghu, Xiao-Liang Qi, C. Honerkamp, and Shou-Cheng Zhang, Topological Mott Insulators, Phys. Rev. Lett. **100**, 156401 (2008).

## Supplementary Material

### A. Orbital angular momentum and the Spin-orbit coupling

In terms of the spherical harmonics $|\ell, m\rangle \equiv Y_\ell^m$, the five atomic $d$-orbitals can be expressed [1] as $\psi^d = V\psi^\ell$, with

$$\psi^d = (d_{YZ}, d_{ZX}, d_{XY}, d_{3Z^2-R^2}, d_{X^2-Y^2})^{\mathrm{T}},$$
$$\psi^\ell = (|2,-2\rangle, |2,-1\rangle, |2,0\rangle, |2,1\rangle, |2,2\rangle)^{\mathrm{T}}, \text{ and}$$
$$V = \begin{pmatrix} 0 & \frac{i}{\sqrt{2}} & 0 & \frac{i}{\sqrt{2}} & 0 \\ 0 & \frac{1}{\sqrt{2}} & 0 & -\frac{1}{\sqrt{2}} & 0 \\ \frac{i}{\sqrt{2}} & 0 & 0 & 0 & -\frac{i}{\sqrt{2}} \\ 0 & 0 & 1 & 0 & 0 \\ \frac{1}{\sqrt{2}} & 0 & 0 & 0 & \frac{1}{\sqrt{2}} \end{pmatrix}.$$

Using the relation $L_\pm = L^x \pm iL^y$, and the angular momentum algebra $L_+|\ell, m\rangle = \sqrt{\ell(\ell+1) - m(m+1)}\ |\ell, m+1\rangle$, $L_-|\ell, m\rangle = \sqrt{\ell(\ell+1) - m(m-1)}\ |\ell, m-1\rangle$, $L^z|\ell, m\rangle = m|\ell, m\rangle$, it is straightforward to obtain the explicit matrix form of the orbital angular moment $\mathbf{L}$ in the $\psi^d$ basis,

$$L^x = \begin{pmatrix} 0 & 0 & 0 & -i\sqrt{3} & -i \\ 0 & 0 & i & 0 & 0 \\ 0 & -i & 0 & 0 & 0 \\ i\sqrt{3} & 0 & 0 & 0 & 0 \\ i & 0 & 0 & 0 & 0 \end{pmatrix},$$

$$L^y = \begin{pmatrix} 0 & 0 & -i & 0 & 0 \\ 0 & 0 & 0 & i\sqrt{3} & -i \\ i & 0 & 0 & 0 & 0 \\ 0 & -i\sqrt{3} & 0 & 0 & 0 \\ 0 & i & 0 & 0 & 0 \end{pmatrix},$$

$$\text{and } L^z = \begin{pmatrix} 0 & i & 0 & 0 & 0 \\ -i & 0 & 0 & 0 & 0 \\ 0 & 0 & 0 & 0 & i2 \\ 0 & 0 & 0 & 0 & 0 \\ 0 & 0 & -i2 & 0 & 0 \end{pmatrix}. \quad \text{(S1)}$$

In order to derive the spin-orbit coupling (SOC), the $d$-orbital basis needs to be enlarged to include the spin degrees of freedom

$$\psi^d = (d_{YZ,\downarrow}, d_{ZX,\downarrow}, d_{XY,\downarrow}, d_{3Z^2-R^2,\downarrow}, d_{X^2-Y^2,\downarrow}, \downarrow\rightarrow\uparrow)^{\mathrm{T}}.$$

The matrix form of the atomic SOC in the $d$-orbital basis is thus given by

$$\mathcal{H}_{\mathrm{SOC}} = \lambda \mathbf{L}\cdot\mathbf{S} = \frac{\lambda}{2}\begin{pmatrix} -L^z & L_+ \\ L_- & L^z \end{pmatrix}. \quad \text{(S2)}$$

It is straightforward to show that the SOC interaction $\mathcal{H}_{\mathrm{SOC}}$ is invariant under joint spin-orbital rotations, *i.e.*, $\mathcal{J}^\dagger(\theta)\mathcal{H}_{\mathrm{SOC}}\mathcal{J}(\theta) = \mathcal{H}_{\mathrm{SOC}}$, where $\mathcal{J}(\theta) = \mathcal{R}_L(\theta)\otimes\mathcal{R}_S(\theta) = e^{iL_z\theta}\otimes e^{iS_z\theta}$ rotates both the orbital and the spin by an angle $\theta$ around the $c$-axis.

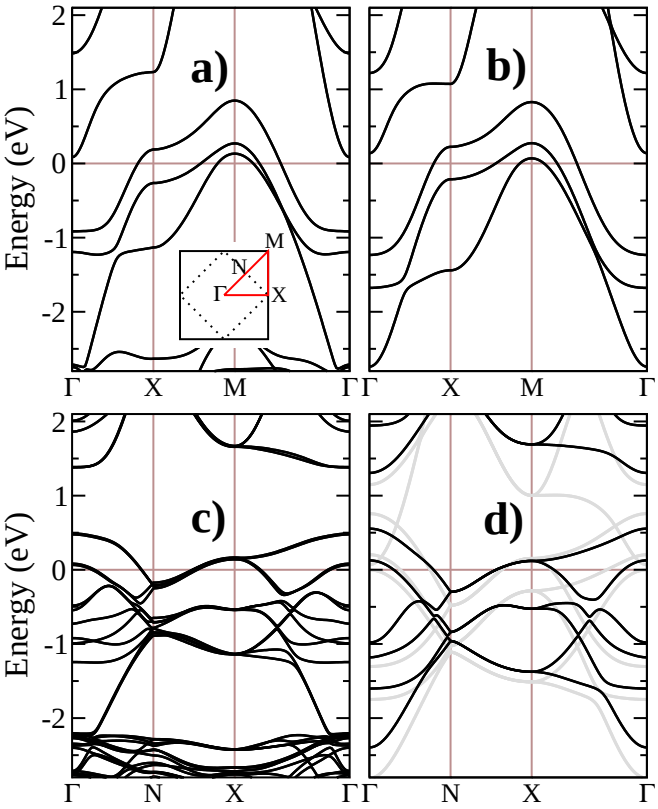


FIG. S1: Comparison between the LDA band structures and the TB+SOC model. (a) LDA without structural distortion. (b) TB+SOC model without structural distortion. (c) LDA with structural distortion. (d) TB+SOC model with structure distortion (black lines). The grey lines in (d) show the band structure in (b) folded into the reduced BZ.

### B. LDA band structure and the TB+SOC model

We first consider an idealized, i.e. *undistorted* $Sr_2IrO_4$ where the staggered rotation of the $IrO_6$ octahedra is neglected. The resulting crystal structure has a space-group of $I4/mmm$ symmetry and the corresponding unit cell contains only one Ir atom. The lattice parameters are from Ref. [2]: $a = b$ =3.89 Å and $c$ =12.92 Å. Taking into account the SOC, the obtained LDA[4] band dispersions is shown in Fig. S1a for the undistorted $Sr_2IrO_4$.

Next, we construct a two-dimensional TB+SOC model for the low-energy band structure using five localized $5d$ Wannier orbitals centered at an Ir site labeled by $\alpha, \beta =$ $1(d_{yz})$, $2(d_{zx})$, $3(d_{xy})$, $4(d_{3z^2-r^2})$, $5(d_{x^2-y^2})$,

$$\tilde{\mathcal{H}}_0 = \sum_{ij,\alpha\beta,\sigma} \tilde{t}_{ij}^{\alpha\beta} d_{i\alpha\sigma}^\dagger d_{j\beta\sigma} + \sum_{i\alpha\sigma} \epsilon_\alpha d_{i\alpha\sigma}^\dagger d_{i\alpha\sigma} + \lambda_{\mathrm{soc}} \sum_{i,\alpha\beta,\sigma\sigma'} \langle \alpha | \mathbf{L} | \beta \rangle \cdot \langle \sigma | \mathbf{S} | \sigma' \rangle\, d_{i\alpha\sigma}^\dagger d_{i\beta\sigma'}. \quad \text{(S3)}$$

Here $d_{i\alpha\sigma}^\dagger$ creates an electron with spin-$\sigma$ in the $\alpha$-th orbital at site $i$. It is important to note that in

TABLE S1: Hopping integrals $\tilde{t}_{\alpha\beta}[\Delta x, \Delta y]$ in units of meV. $[\Delta x, \Delta y]$ denotes the in-plain hopping vector, and $(\mu, \nu)$ the orbitals. **I**, $\sigma_y$, and $\sigma_d$ correspond to $\tilde{t}_{\alpha\beta}[-\Delta x, -\Delta y]$, $\tilde{t}_{\alpha\beta}[\Delta x, -\Delta y]$, and $\tilde{t}_{\alpha\beta}[\Delta y, \Delta x]$, respectively, where "$\pm$" and "$\pm(\alpha', \beta')$" in the row of $(\alpha, \beta)$ mean that the corresponding hopping is equal to $\pm\tilde{t}_{\alpha\beta}[\Delta x, \Delta y]$ and $\pm\tilde{t}_{\alpha'\beta'}[\Delta x, \Delta y]$, respectively. This table, combined with the relation $\tilde{t}_{\alpha\beta}[\Delta x, \Delta y] = \tilde{t}_{\beta\alpha}[-\Delta x, -\Delta y]$, gives all the $ab$-plane hoppings $\geq$ 1meV up to fifth neighbors.

| $(\alpha, \beta)$ | [1,0] | [1,1] | [2,0] | [2,1] | [2,2] | **I** | $\sigma_y$ | $\sigma_d$ |
|---|---|---|---|---|---|---|---|---|
| (1,1) | −66 | 16 | 12 | 5 | 2 | + | + | +(2,2) |
| (1,2) | | 3 | | 1 | −2 | + | − | + |
| (2,2) | −391 | 16 | 30 | 6 | 2 | + | + | +(1,1) |
| (3,3) | −391 | −139 | 30 | −10 | −11 | + | + | + |
| (3,4) | | 88 | | 11 | 9 | + | − | + |
| (3,5) | | | | −12 | | + | − | − |
| (4,4) | −245 | −38 | −6 | −3 | −1 | + | + | + |
| (4,5) | 309 | | 30 | 8 | | + | + | − |
| (5,5) | −792 | 173 | −140 | 3 | | + | + | + |

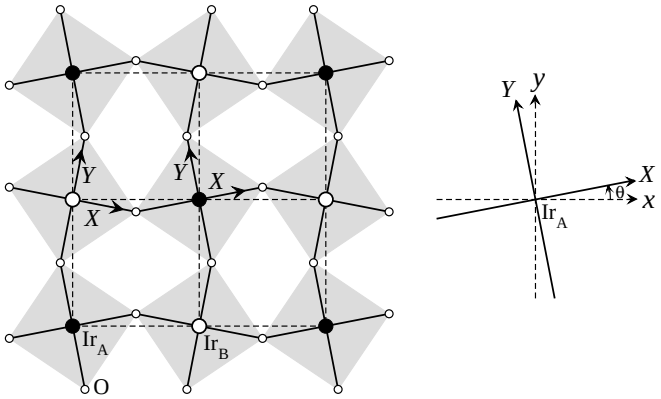


FIG. S2: Schematic picture of a $IrO_2$ layer. Large filled or open circles denote Ir atoms on two sublattices, and small open circles are oxygen atoms. Small $x$, $y$ are the global cubic axis, while capital $X$, $Y$ denote local sublattice-dependent axis. The $IrO_6$ octahedra of sublattice A/B are rotated about $c$-axis by $\theta = \pm 11^\circ$.

Eq. (S3), the spin and orbital are defined in the *global* coordinates $(x, y, z)$ of the system. The hopping integrals $\tilde{t}_{ij}^{\alpha\beta} \equiv \tilde{t}_{\alpha\beta}[x_j - x_i, y_j - y_i]$ are *real* and given in table S1 for up to fifth nearest neighbors. The obtained crystalline electric field (CEF) hierarchy is given by $\epsilon_{1,\cdots,5} = (0, 0, 202, 3054, 3831)$ meV. The last term in Eq. (S3) describes the atomic SOC and the matrix representation is given explicitly in Eq. (S2). The LDA value for the atomic SOC is $\lambda_{\rm soc} = 357$ meV. The band dispersion produced by the TB+SOC Hamiltonian is shown in Fig. S1b, which captures faithfully the low-energy part of the LDA band structure in Fig. S1a.

In realistic $Sr_2IrO_4$ materials, the corner-shared $IrO_6$ are not well-aligned but are alternately rotated clockwise and anticlockwise around the $c$-axis by about 11°. The top view of the staggered octahedral rotation is shown schematically in Fig. S2, which lowers the symmetry group of $Sr_2IrO_4$ from $I4/mmm$ to $I4_1/acd$ and the corresponding primitive unit cell contains four ($\sqrt{2}\times\sqrt{2}\times 2$) formula units. The lattice constants we used here are taken from the values obtained at 295 K by Crawford *et. al.* [3]: $a = b$ =5.497 Å($a_t$ =3.887 Å), $c$ =25.798 Å($c_t$ =12.899 Å). The obtained LDA band structure near the Fermi level is shown in Fig. S1c in the reduced zone in two dimensions (2D) plotted in the inset in Fig. S1a since the staggered octahedral rotation doubles the 2D unit cell. It clearly deviates from the grey lines in Fig. S1d obtained by simply folding the band structure of the TB+SOC model in Eq. (S3) into the 2D reduced BZ. The main difference is that the band crossing (mainly $d_{xy}$ and $d_{x^2-y^2}$ orbitals) above the Fermi level near Γ is lifted by the structure distortion.

In order to obtain the tight-binding model in the presence of the structure distortion, it is essential to transform the atomic spin/orbital into the *local* coordinates that follow the staggered octahedral rotation. The SOC term is invariant as shown in the last section. Assuming the atomic crystal fields in the local $IrO_6$ environment are unchanged to a good approximation, the main effects of the octahedral rotation is on the hopping term in Eq. (S3). This amounts to a spatial rotation from the global $(x, y, z)$ to the local $(X, Y, Z)$ coordinates shown in Fig. S2 by angles $\theta_i$ and a spin rotation by angles $\theta_i$ [5], i.e. $\mathcal{R}_i = e^{-iL_z\theta_i} \otimes e^{iS_z\theta_i}$. The hopping of an electron from site $j$ to site $i$ is described by the $10 \times 10$ matrix, $\tilde{t}_{ij}$, in the spin-orbital space. Carrying out this rotation on the hopping matrix, $t_{ij} = \mathcal{R}_i^\dagger \tilde{t}_{ij} \mathcal{R}_j$, one finds that the hopping matrix $t_{ij}$ is in general *complex* and spin-orbital dependent but diagonal in spin space. The TB+SOC model in the local $(X, Y, Z)$ coordinates is thus given by

$$\mathcal{H}_0 = \sum_{ij,\mu\nu,\sigma} t_{ij}^{\mu\nu,\sigma} d_{i\mu\sigma}^\dagger d_{j\nu\sigma} + \sum_{i\mu\sigma} \epsilon_\mu d_{i\mu\sigma}^\dagger d_{i\mu\sigma} + \lambda_{\rm soc} \sum_{i,\mu\nu,\sigma\sigma'} \langle \mu \,|\mathbf{L}|\, \nu \rangle \cdot \langle \sigma \,|\mathbf{S}|\, \sigma' \rangle \, d_{i\mu\sigma}^\dagger d_{i\nu\sigma'}, \quad \text{(S4)}$$

where the orbital indices $\mu, \nu = 1(d_{YZ}), 2(d_{ZX}), 3(d_{XY}), 4(d_{3Z^2-R^2}), 5(d_{X^2-Y^2})$, as given in Eq. (1) in the main text. The obtained band dispersion is shown as black lines in Fig. S1d, which provides an accurate five-orbital TB+SOC description of the LDA band structure in the presence of lattice distortion shown in Fig. S1c.

### C. $J_{\rm eff} = 1/2$ bands

Since the cubic crystal field $\Delta_c = 10Dq$ ($\simeq$ 3.4 eV) is much larger than $\lambda_{\rm soc}$, the five $d$ atomic orbitals split into the 3-fold $t_{2g}$ manifold consisting of $d_{YZ}$, $d_{ZX}$, and $d_{XY}$, and the higher lying 2-fold $e_g$ manifold of $d_{3Z^2-R^2}$ and $d_{X^2-Y^2}$. Projecting out the high energy $e_g$ manifold, it has been shown [6, 7] that the $t_{2g}$ manifold has an

effective angular moment $\ell = 1$ with triplets $|1,0\rangle = d_{XY}$, $|1,\pm1\rangle = -\frac{1}{\sqrt{2}}(id_{ZX} \pm d_{YZ})$ and reversed angular momentum $\mathbf{L} \to -\mathbf{L}$. The truncated matrix form of the SOC in the $t_{2g}$ manifold thus reads

$$\mathcal{H}_{\rm SOC} = -\lambda \mathbf{L}\cdot\mathbf{S} = \frac{\lambda}{2}\left(\begin{array}{ccc|ccc} 0 & -i & 0 & 0 & 0 & 1 \\ i & 0 & 0 & 0 & 0 & i \\ 0 & 0 & 0 & -1 & -i & 0 \\ \hline 0 & 0 & -1 & 0 & i & 0 \\ 0 & 0 & i & -i & 0 & 0 \\ 1 & -i & 0 & 0 & 0 & 0 \end{array}\right) \quad \text{(S5)}$$

in the basis of $(d_{YZ,\downarrow},\ d_{ZX,\downarrow},\ d_{XY,\downarrow};\ \downarrow\to\uparrow)^T$. The SOC further splits the $t_{2g}$ complex into spin-orbit multiplets with a $J_{\rm eff} = 3/2$ quartet and a higher lying $J_{\rm eff} = 1/2$ doublet. The $J_{\rm eff} = 1/2$ doublet is given by

$$|\frac{1}{2},\frac{1}{2}\rangle = \frac{1}{\sqrt{3}}\left(id_{YZ,\downarrow} + d_{ZX,\downarrow} + id_{XY,\uparrow}\right), \text{ and}$$
$$|\frac{1}{2},-\frac{1}{2}\rangle = \frac{1}{\sqrt{3}}\left(-id_{YZ,\uparrow} + d_{ZX,\uparrow} + id_{XY,\downarrow}\right).$$


[1] https://en.wikipedia.org/wiki/Table_of_spherical_harmonics

[2] J.J. Randall, Lewis Katz, and Roland Ward, The Preparation of a Strontium-Iridium Oxide $Sr_2IrO_4$. J. Am. Chem. Soc. **79**, 266 (1957).

[3] M.K. Crawford *et. al.*, Structural and magnetic studies of $Sr_2IrO_4$, Phys. Rev. B **49**, 9198 (1994).

[4] P. Giannozzi *et. al.*, QUANTUM ESPRESSO: a modular and open-source software project for quantum simulations of materials, J. Phys.: Condens. Matter **39**, 395502 (2009).

[5] Fa Wang and T. Senthil, Twisted Hubbard Model for $Sr_2IrO_4$: Magnetism and Possible High Temperature Superconductivity, Phys. Rev. Lett. **106** 136402 (2011).

[6] A. Abragam and B. Bleaney, Electron Paramagnetic Resonance of Transition Ions. Clarendon Press, Oxford, (1970).

[7] G. Jackeli and G. Khaliullin, Mott Insulators in the Strong Spin-Orbit Coupling Limit: From Heisenberg to a Quantum Compass and Kitaev Models, Phys. Rev. Lett. **102**, 017205 (2009).